

TRANSITION REGION AND CHROMOSPHERIC SIGNATURES OF IMPULSIVE HEATING EVENTS. I. OBSERVATIONS

HARRY P. WARREN¹, JEFFREY W. REEP², NICHOLAS A. CRUMP³, PAULO J. A. SIMÕES⁴

To be submitted to the Astrophysical Journal

ABSTRACT

We exploit the high spatial resolution and high cadence of the Interface Region Imaging Spectrograph (IRIS) to investigate the response of the transition region and chromosphere to energy deposition during a small flare. Simultaneous observations from RHESSI provide constraints on the energetic electrons precipitating into the flare footpoints while observations of XRT, AIA, and EIS allow us to measure the temperatures and emission measures from the resulting flare loops. We find clear evidence for heating over an extended period on the spatial scale of a single IRIS pixel. During the impulsive phase of this event the intensities in each pixel for the Si IV 1402.770 Å, C II 1334.535 Å, Mg II 2796.354 Å, and O I 1355.598 Å emission lines are characterized by numerous, small-scale bursts typically lasting 60 s or less. Red shifts are observed in Si IV, C II, and Mg II during the impulsive phase. Mg II shows red-shifts during the bursts and stationary emission at other times. The Si IV and C II profiles, in contrast, are observed to be red-shifted at all times during the impulsive phase. These persistent red-shifts are a challenge for one-dimensional hydrodynamic models, which predict only short-duration downflows in response to impulsive heating. We conjecture that energy is being released on many small-scale filaments with a power-law distribution of heating rates.

Subject headings: Sun: corona, sun: transition region, sun: flares

1. INTRODUCTION

Understanding how the solar upper atmosphere is heated to high temperatures is a fundamental problem in solar physics. It has long been recognized that the solar chromosphere and transition region, which supply the corona with mass, should provide important diagnostic information on the energy release mechanism. The complex topology and rapid evolution of these layers of the solar atmosphere, however, has made this difficult to achieve in practice.

Recent observations from the High Resolution Coronal Imager (Hi-C, Cirtain et al. 2013) and the Interface Region Imaging Spectrograph (IRIS, De Pontieu et al. 2014) suggest that at sufficiently high spatial and temporal resolution it is possible to track the response of the transition region and chromosphere to some individual heating events. For example, Testa et al. (2013) showed that at the approximately 150 km spatial resolution and 5.5 s cadence of Hi-C, temporal variability in active region loop footpoints (the “moss,” e.g., Berger et al. 1999) associated with the heating of some high temperature loops becomes apparent. Lower resolution observations of the moss, in contrast, had suggested that the heating was relatively steady (e.g., Antiochos et al. 2003; Brooks & Warren 2009). Similarly, Testa et al. (2014) identified several events in 9.5 s cadence IRIS sit-and-stare observations that showed strong blueshifts in Si IV. Numerical simulations indicate that these blueshifts are a signature of energy deposition at heights below the region where Si IV is typically formed, perhaps because the energy transport in these events is driven by electron beams rather than thermal conduction. This recent work sug-

gests that a detailed examination of the transition region and chromosphere is likely to yield new insights into the physics of energy release during flares.

There is, of course, a long history of both observational and theoretical studies of impulsive flare dynamics (for a review see Fletcher et al. 2011). Previous observations have established the close correspondence between the evolution of hard X-ray emission and emission from the transition region and chromosphere (e.g., Kane & Donnelly 1971; Cheng et al. 1981; Poland et al. 1982; Woodgate et al. 1983; Tandberg-Hanssen et al. 1983; Hudson et al. 1994; Simões et al. 2015) as well as the presence of both evaporative upflows at high temperatures (e.g., Doschek et al. 1980; Antonucci et al. 1982) and downflows at transition region and chromospheric temperatures (e.g., Ichimoto & Kurokawa 1984; Zarro et al. 1998; Canfield et al. 1990).

Early numerical simulations were able to reproduce the very high coronal temperatures and densities associated with impulsive energy deposition and chromospheric evaporation (e.g., Nagai 1980; Fisher et al. 1985; Mariska et al. 1989). These models were also able to account for the red-shifts observed in the chromosphere and transition region, which are a consequence of the sudden evaporative upflows at higher temperatures and momentum conservation (Fisher 1989). As discussed by Emslie & Alexander (1987), however, these numerical simulations also predicted that the evaporative upflows should dominate the velocity signature and the observed line profile should be completely blueshifted. This is rarely observed in spatially unresolved observations (Mariska et al. 1993). At the spatial resolution of several thousand kilometers some completely blueshifted high temperature profiles are observed (e.g., Czaykowska et al. 2001; Doschek et al. 2013). At the approximately 200 km spatial resolution of IRIS, completely blueshifted Fe XXI emission is observed routinely (Tian et al. 2014; Young et al. 2015; Tian et al. 2015; Graham & Cauzzi 2015; Polito et al. 2016). This discrepancy is a consequence of the filamentary nature of energy release

¹ Space Science Division, Naval Research Laboratory, Washington, DC 20375

² National Research Council Postdoctoral Fellow, Space Science Division, Naval Research Laboratory, Washington, DC 20375

³ Naval Center for Space Technology, Naval Research Laboratory, Washington, DC 20375

⁴ SUPA School of Physics and Astronomy, University of Glasgow, Glasgow G12 8QQ, UK

during a flare (Hori et al. 1997; Reeves & Warren 2002; Warren 2006).

In this paper we investigate the evolution of transition region and chromospheric line intensities, velocities, and widths observed with a high cadence IRIS sit-and-stare observation of a small event (GOES class B4 after background subtraction) that occurred on 19 November 2014. The combination of data from many different satellites allows us to measure comprehensively the properties and dynamics of the event in ways not possible with any individual instrument. We enumerate the constraints and observables that a model must be able to reproduce in order to sufficiently understand the energy release. This paper is part of a larger program to understand the relationship between transition region emission and energy deposition in small events such as microflares in the hope that these properties can be extrapolated to events that heat the solar corona.

2. OBSERVATIONS

IRIS is a compact spectrograph based on a Cassegrain design. Special coatings allow for simultaneous imaging of the 1332–1407 and 2783–2835 Å wavelength ranges. The far UV (FUV) wavelength range includes strong emission lines from O I 1355.598, C II 1334.535 and 1335.708, Si IV 1393.755 and 1402.770, O IV 1399.775 and 1401.163, Fe XII 1349.382, and Fe XXI 1354.080 Å. The near UV (NUV) wavelength range includes Mg II k 2796 and Mg II 2803 Å lines. The nearly 7 m effective focal length provides a spatial resolution scale of $0''.33$ or about 230 km. Spectroscopy is provided by passing solar radiation through a $0''.33 \times 175''$ slit and reflecting it off of a grating. The resulting spectral resolution is about 26 mÅ in the FUV and 53 mÅ in the NUV. Light reflected off of the slit assembly is passed through one of four science filters to allow for context imaging of an area $175'' \times 175''$ around the slit. The high effective area of IRIS relative to previous spectrographs allows for much higher observing cadences, which are typically below 10 s. IRIS was launched into a sun-synchronous orbit and nearly continuous observing is possible for about 9 months of the year. For additional details on the instrument see De Pontieu et al. (2014).

The large volume of data returned by IRIS makes it difficult to inspect every observation. To filter the data we cross-referenced the flare catalog provided by the The Reuven Ramaty High Energy Solar Spectroscopic Imager (Lin et al. 2002, RHESSI) with the IRIS observation catalog to find flares for which there was RHESSI emission within the IRIS slit-jaw field of view. We then created quick-look movies of the IRIS slit-jaw data and evaluated the events individually.

The microflare that occurred on 19 November 2014 beginning at about 14:14 UT is particularly well observed. In addition to data from IRIS and RHESSI there are simultaneous observations from the Extreme Ultraviolet Imaging Spectrometer (EIS, Culhane et al. 2007), the X-Ray Telescope (XRT, Golub et al. 2007), and the Atmospheric Imaging Assembly (AIA, Lemen et al. 2012). These data provide important constraints on the physical properties in the loops that ultimately form above the footpoint regions observed with IRIS and RHESSI. The spectral lines observed with EIS, for example, provide information on both the high-temperature loops through the observation of emission from Ca XVII, Fe XXIII, and Fe XXIV and the pressure in the loops through the Fe XIV density diagnostic. These observations are typically taken at relatively low cadence, with spectra taken at

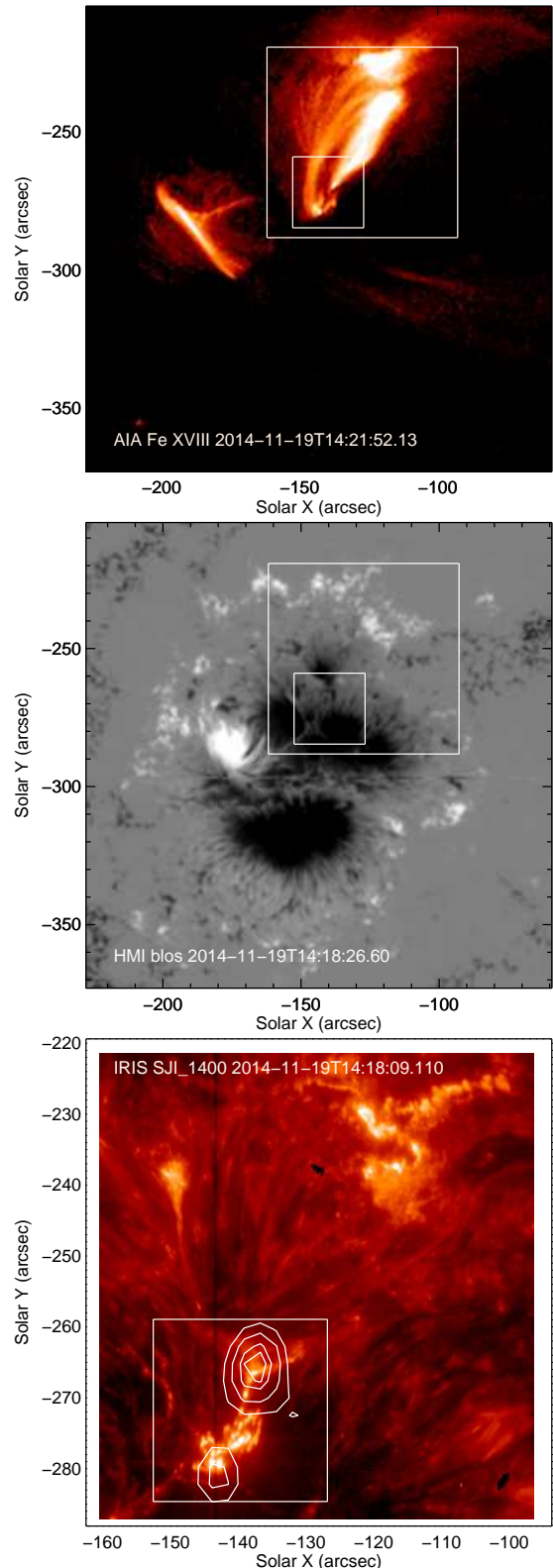


FIG. 1.— AIA Fe XVIII, HMI line-of-sight magnetogram, and IRIS 1400 Å slit-jaw images taken near the peak of a small event, SOL2014-11-19T14:25 UT. The peak GOES flux was about C1.1 and the event was not recorded as a flare on the GOES event list. RHESSI 15–25 keV contours are shown on the IRIS slit-jaw image. The dark vertical feature in the IRIS slit-jaw image is the shadow of the slit. The small white box indicates the field of view shown in Figures 2, 5, and 11 and highlights the footpoint region near the sunspot penumbra.

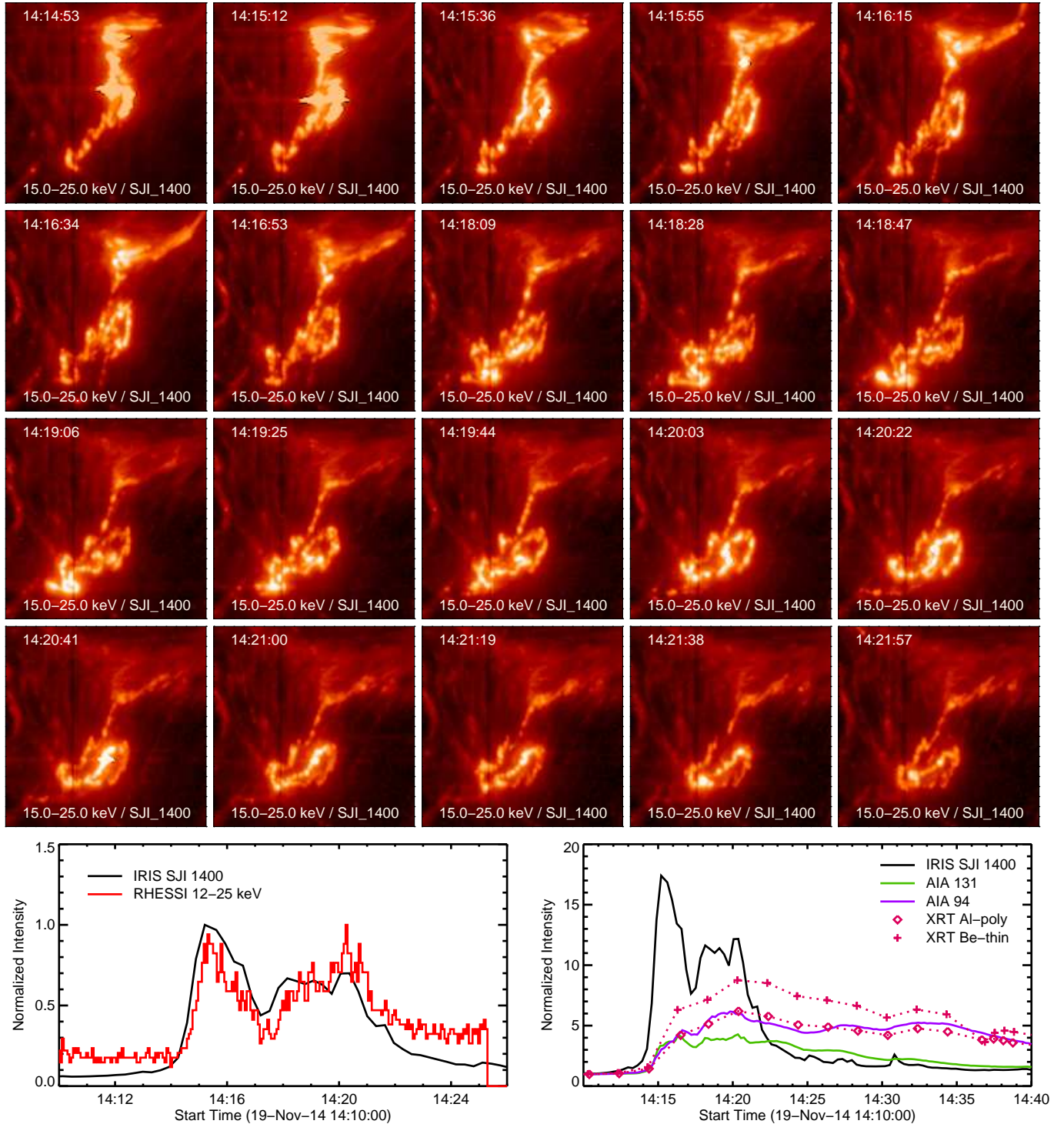


FIG. 2.— (*top panels*) The evolution of flare footpoints observed with IRIS. The field of view shown is $26'' \times 26''$ in size. (*bottom left panel*) The total intensity in the IRIS slit jaw and in RHESSI as a function of time. Note that the IRIS intensities are taken only from this small field of view while the RHESSI fluxes are not spatially resolved. Each light curve is normalized to its maximum. (*bottom right panel*) The total intensity in IRIS, AIA 94 Fe XVIII, AIA 131 Fe XXI, XRT Al-poly/Open, and XRT Be-thin/Open for the small field of view. Here each light curve is normalized to the intensity at the start of the observations.

one position every few minutes. Observations from XRT and AIA in the 131 Å and 94 Å channels, which observe Fe XXI 128.75 Å and Fe XVIII 93.93 Å, provide information on the high-temperature emission on much shorter time scales (for a discussion of the XRT and AIA temperature responses see O'Dwyer et al. 2014, 2010).

2.1. Observations of the Flare Footpoints

In Figure 1 we show an AIA 94 Å image, HMI line-of-sight magnetogram, and IRIS 1400 Å slit-jaw image from the event, which occurred in the vicinity of a sunspot. The AIA 94 Å image has been processed to remove some of the contaminating

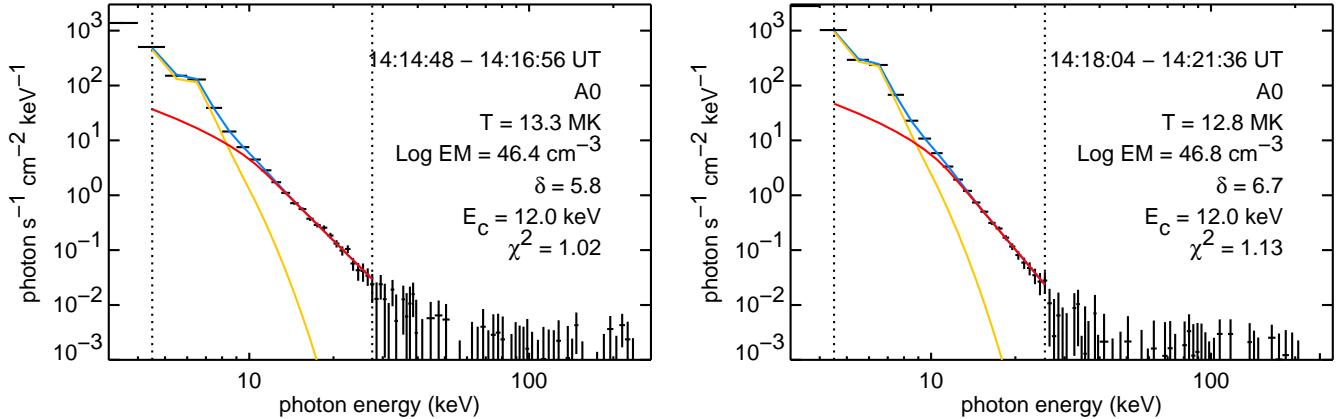


FIG. 3.— RHESSI spectral fits of the two main peaks of the flare.

1 MK emission and emphasize Fe XVIII (Warren et al. 2012). The larger AIA and HMI images indicate the field of view for the IRIS slit-jaw image. For the period between 14:08 and 15:03 UT IRIS alternated taking slit-jaw images in the 1400 Å and 1335 Å channels. The cadence for each channel was about 19 s.

The co-alignment of the various observations is an important component of this work. Unfortunately the pointing information specified in most of the file headers is not accurate enough to co-register these data. We have assumed that the AIA data have the most accurate pointing and have written software to cross-correlate the IRIS, XRT and EIS observations to it. The relatively high cadence of AIA — the standard 12 s for EUV images and 24 s for UV images was used during these observations — insures that image pairs are always close together in time. For the IRIS slit-jaw images we co-align using AIA 1600 Å, for XRT we use AIA 94 Å, and for EIS 195.119 Å we use AIA 195 Å. For the lower resolution XRT and EIS data, blinking the images indicates that this procedure works very well. For the IRIS data it is able to correct for longer-term pointing drifts in the image sequence but does introduce some jitter that is evident in the animations of the data. We note that no adjustments to the RHESSI pointing appear to be necessary.

The IRIS slit-jaw images for this period show intense brightenings in the sunspot penumbra and in some of the near-by opposite polarity flux. To investigate the relationship between these brightenings and the hard X-ray emission we have computed a RHESSI 15–25 keV image using the “clean” algorithm (Hurford et al. 2002) with a 2.4'' pixel size and a 240 s integration centered on the time of each IRIS slit-jaw image. The long integration time relative to the cadence of the IRIS slit-jaw observations is necessary to bring up the signal-to-noise. Only detectors 3, 6, 8, and 9 are used for these image reconstructions. Except for the `clean_beam_width_factor`, which we set to 1.5 to narrow the spatial extent of the beam, we use the default RHESSI imaging parameters for the clean algorithm.

The RHESSI images indicate that most of the hard X-ray emission comes from the footpoints rooted in the strong magnetic field of the sunspot penumbra. Figure 1 shows the contours of the RHESSI emission superimposed on an IRIS slit-jaw image. The lowest intensity RHESSI contour shown is about a factor of two smaller than the peak. Lower intensity

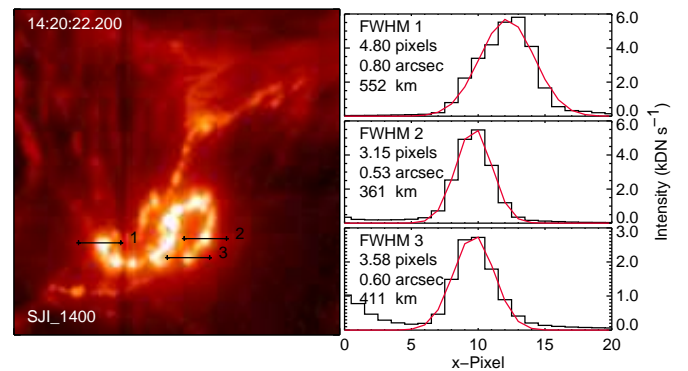


FIG. 4.— Cross-sectional profiles of IRIS footpoint intensities at 14:20 UT. The left panel shows cross-sectional lines through three footpoint brightenings. The right panel shows the corresponding intensity profiles and FWHM.

values show features that are clearly unrelated to the structures seen in the IRIS images and likely to be noise generated from the inversion.

In Figure 2 we show individual IRIS slit-jaw images as well as light curves computed by summing the IRIS intensities over the small region of interest and integrating all of the available RHESSI counts. As expected, these light curves show a close relationship between the transition region intensity and the hard X-ray emission. The images and light curves show that hard X-ray emission is concentrated into two bursts that peak at approximately 14:15 and 14:20 UT. Isothermal fits to the RHESSI spectra for times centered around these peaks are shown in Figure 3. Here the `vth+thick2_vnorm` model is used. This model describes an isothermal component plus a non-thermal component produced by thick target bremsstrahlung from a power-law distribution of electrons. It is part of the standard spectral analysis software for RHESSI (Schwartz et al. 2002).

The best-fit temperatures, which will be relevant to the discussion of the temperatures derived from the XRT, EIS, and AIA observations later in the paper, are 13.3 ± 0.4 and 12.8 ± 0.3 MK. The spectral indexes for the non-thermal component of the electrons for these times are 5.8 ± 0.1 and 6.7 ± 0.2 , and are important parameters in modeling the energy deposition in these footpoint regions.

The differences in spatial resolution between the two instruments are readily apparent here. The broad regions of hard X-ray emission are imaged as many small footpoint brighten-

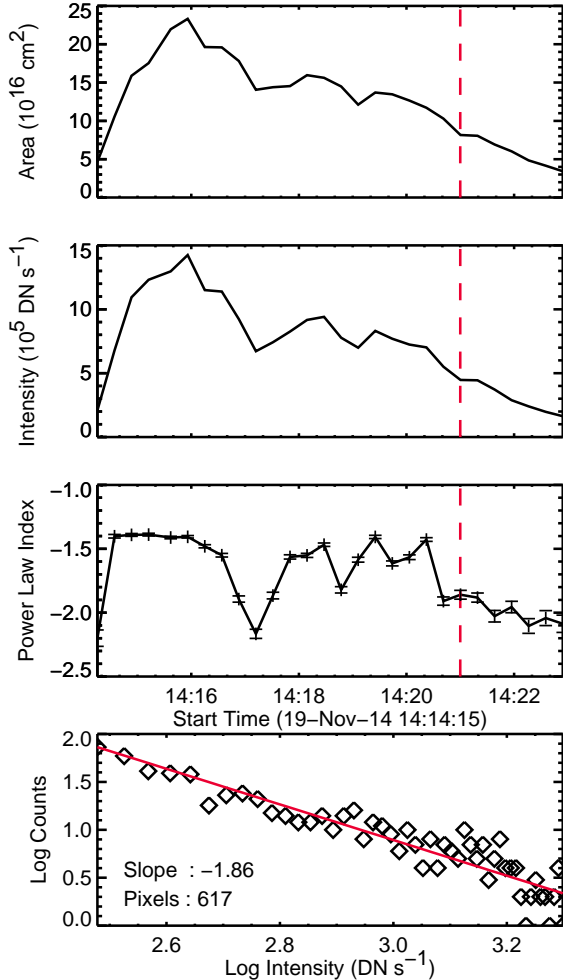


FIG. 5. — The distribution of IRIS footpoint intensities at 14:21 UT (bottom panel). The top panels show the total footpoint area, the total footpoint intensity, and the power-law index of the footpoint intensity as functions of time. These quantities are derived from the footpoints near the sunspot penumbra.

ings in IRIS. As shown in Figure 4, the footpoints observed in IRIS typically have a FWHM of about $0''.6$ or about 410 km. Equally important is the difference in dynamic range. The IRIS detector records data values to 14 bits (0 to 16,383 or about 4 orders of magnitude) while RHESSI has a dynamic range of about a factor of two in this event.

The strong correlation between the transition region and hard X-ray emission suggests that we can gain additional insight into the distribution of heating intensity along footpoints by measuring the distribution of IRIS intensities there. We measured this distribution for the duration of the hard X-ray burst, finding it well described by a power-law and well correlated with the hard X-ray intensity. The intensity histogram for an IRIS image taken near the second hard X-ray peak shown in Figure 5 illustrates the power-law distributions that are observed in the footpoints. The indexes on these distributions range between -1.5 and -2.5 and have a median value of about -1.6. Note that this index is fundamentally different than the spectral index on the non-thermal electron distribution. This index describes how the energy released during the flare is distributed across different field lines while the spectral index describes how energy is distributed across all of the electrons.

The IRIS slit provides another view on the physical conditions in the footpoints. During this period the slit was kept in a fixed position and spectra were recorded at a cadence of about 9.5 s. To make the data easier to visualize we computed moments for each line profile. The moments are defined as

$$I = \sum_{i=1}^N I_i \quad (1)$$

$$\lambda_0 = \frac{1}{I} \sum_{i=1}^N \lambda_i I_i \quad (2)$$

$$\sigma = \frac{I \Delta}{\max(I_i) \sqrt{2\pi}}, \quad (3)$$

where I_i is the background subtracted intensity in units of DN s^{-1} and Δ is the width of a spectral pixel. This alternative definition of the width moment is used because it yields better performance for low count rates. We chose to compute moments instead of fitting the profiles because the moment calculation is much faster and, as we will see, the profiles are not particularly well represented by a single Gaussian. We could fit multiple Gaussians to these profiles, but such fits are often poorly constrained.

We focus on the moment calculations for Si IV 1402.770 Å, C II 1334.535 Å, and O I 1355.598 Å. These lines are formed at progressively lower temperatures. In ionization equilibrium, Si IV peaks at $\log T = 4.8$, C II at 4.4, and O I at or below 4.0. We also consider the spectral region near the Mg II h & k doublet, which is sensitive to a wide range of temperatures in the solar chromosphere (e.g., Pereira et al. 2013). These spectral features are optically thick and often show a strong reversal in the core of the line (e.g., Schmit et al. 2015). As we will see, the profiles are not reversed during this flare and the Gaussian moment is an adequate description of the line profile. We take the rest wavelengths for the doublet, 2796.354 Å for the k-line and 2803.531 Å for the h-line, from Murphy & Berengut (2014). Fitting time-averaged profiles from the sunspot in this observation yields velocities of less than 1 km s^{-1} with these wavelengths.

We also investigated Fe XII 1349.382 Å (6.2) and Fe XXI 1354.080 Å (7.05), but did not detect emission in these lines. We will discuss the coronal component of these observations in section 2.2.

In Figure 6, 7, and 8 we show the intensity, Doppler velocity, and width as a function of space and time for the Si IV, C II, and Mg II lines. The results for O I are not shown. These data are taken from the region around the southern brightening, which is the only flare-related emission observed along the slit.

During the event the intensity in Si IV rises by about a factor of 1000, the intensity in C II rises by about a factor of 100, and the Mg II and O I intensity rises by a factor of 10. During the initial part of the event, from approximately 14:14 to 14:24 UT, numerous increases in the intensity lasting about 30 s are observed. These intensity bursts are well correlated among the various emission lines. After about 14:24 UT there is a slow decay phase during which the fluctuation level in the intensity of all of the lines is much lower.

During the event we also observe systematic red shifts in Si IV and C II. In Si IV the red shifts are typically $10\text{--}40 \text{ km s}^{-1}$. In C II the red-shifts are somewhat smaller, at $5\text{--}30 \text{ km s}^{-1}$. Mg II shows red shifts associated with the

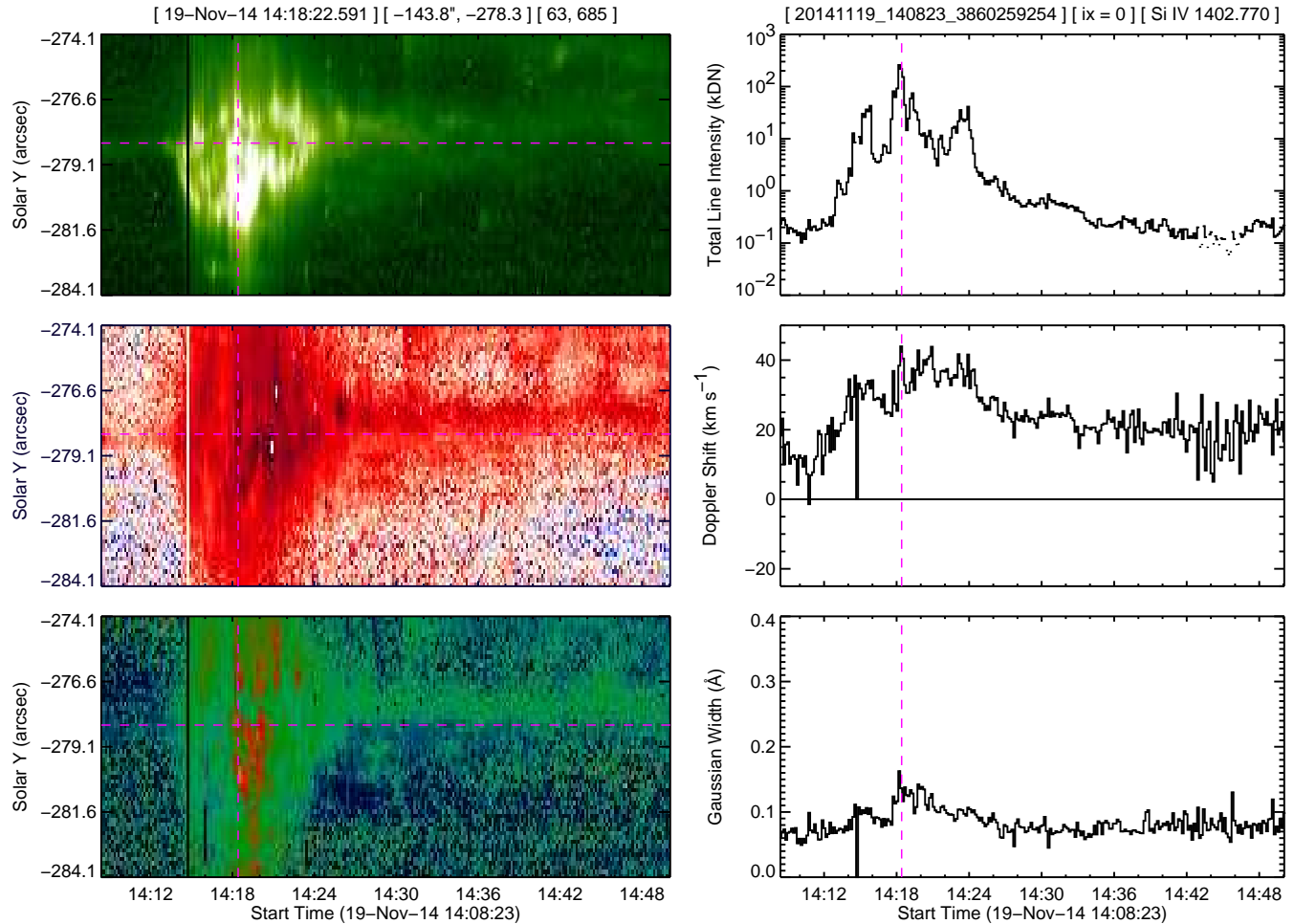


FIG. 6.— Intensities, Doppler shifts, and Gaussian line widths determined from moments of the Si IV 1402.770 Å line. The line profiles are red-shifted at almost all times from about 14:14 to 14:24, and some regions show red-shifts to 14:50. The left panels show these quantities as a function of position along the slit and time. The region along the slit corresponds to the brightenings seen near the sun spot penumbra. Note that the values listed in brackets above these panels indicate the position of the horizontal line in both absolute coordinates co-aligned to AIA (-143.8'', -278.3'') and in the pixel coordinates of the data array (63, 685). The right panels show these quantities for a single slit position as a function of time. The vertical line indicates 2014 November 19 14:18:22.591 UT.

strongest bursts. The O I line shows essentially no change in velocity during the flare. This line typically shows a blue shift of about 2 km s^{-1} at all times, which likely reflects the uncertainty in the wavelength calibration.

The red-shifts observed in Si IV and C II persist at elevated levels throughout the early part of the event. From approximately 14:14 to 14:24 UT almost all of the intense emission in these lines is red-shifted. After this time, the persistent red-shifts appear to be more localized. There is a region around $y \sim -277''$ where the red-shifts last beyond 14:50 UT in both lines.

For Si IV and C II we also observe changes in the line width during the event. These changes are similar in magnitude for both lines and well correlated with the intensity fluctuations. In contrast with the Doppler shift, the line width observed for Si IV and C II is close to the pre-flare value during the decay of the event. Again, O I behaves differently, showing essentially no change in width during the flare.

The moments give us a sense of how the bulk properties of the line profiles are evolving during the flare, but they also act to compress the data and may obscure important spectral features. We have not, for example, attempted to account for any unrelated emission along the line of sight and the observed

profile could be a mixture of flare and non-flare components.

In Figure 9 we display Si IV, C II, and Mg II line profiles as a function of time at a single spatial location. Here we see the line profiles appear to be composed of two or more distinct components. We also see that the emission in these components is significantly enhanced over the background at all wavelengths during the flare. For Si IV, one of the components typically has a velocity of about 20 km s^{-1} while the other is at about 40 km s^{-1} . C II also exhibits multiple components, but one is typically at rest while the other primary component is typically at about $20\text{--}40 \text{ km s}^{-1}$. The Mg II profiles are similar to those of C II. As is suggested by the lack of variation in the width, O I does not show any complex dynamical evolution in the line profile.

The final piece of information on the physical conditions in the footpoints that we have considered comes from the EIS electron densities inferred from the Fe XIV 264.787/274.203 Å ratio. As is indicated by the theoretical ratio taken from version 8 of CHIANTI (Del Zanna et al. 2015), this line ratio is sensitive to density up to about $\log n_e = 11$. Since this ion is formed at about 2 MK, this ratio can measure pressures to about $\log P = 2n_e T_e = 17.6$, where the pressure has units of $\text{cm}^{-3} \text{ K}$. The EIS observations for this period

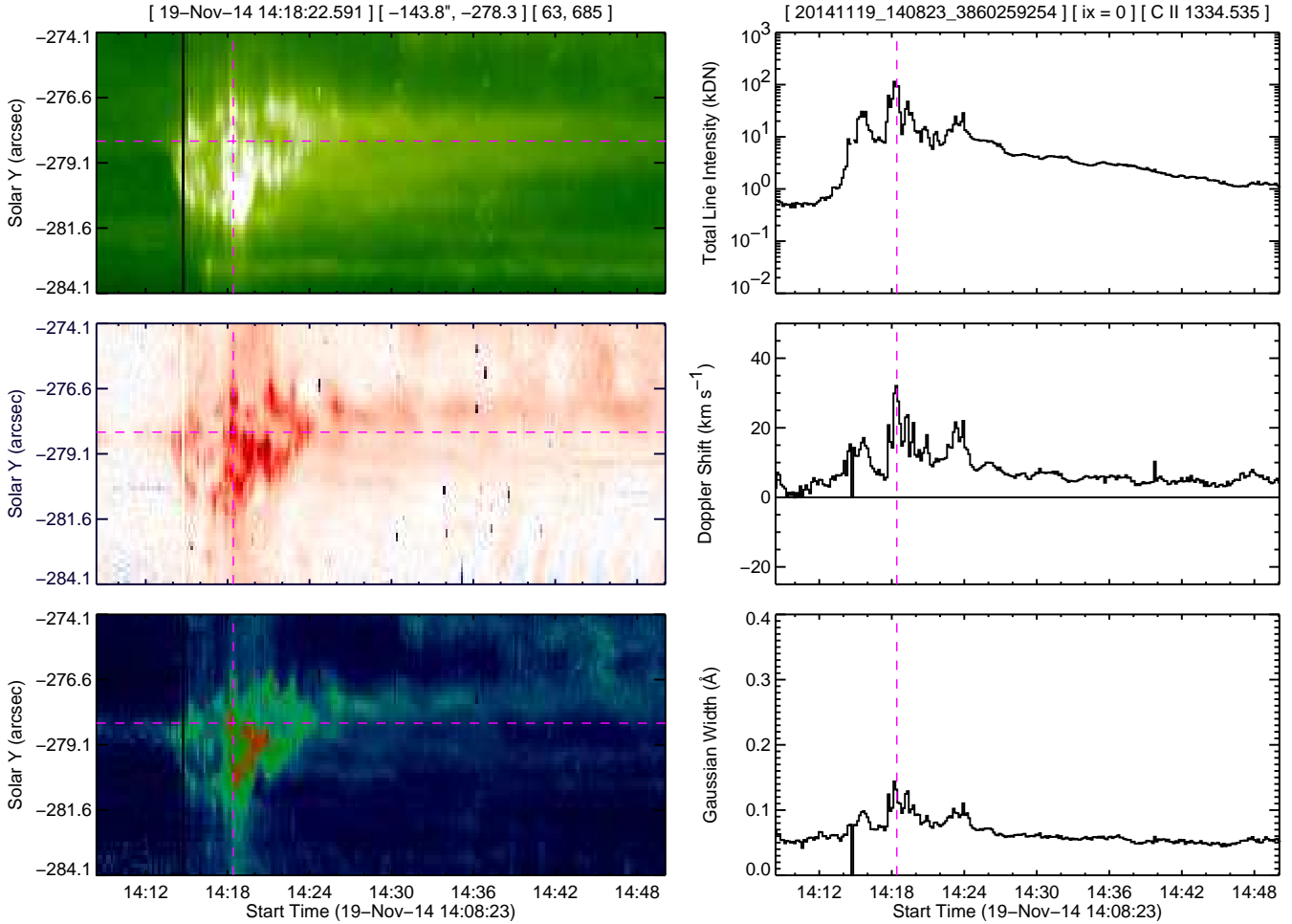


FIG. 7.— The same format as Figure 6 but for the C II 1334.535 Å line. The variations in intensity, Doppler shift, and line width are well correlated with those measured for Si IV, but the magnitude of the response is somewhat smaller.

consisted of a sparse scan across the active region using $3''$ steps. The spatial resolution along the slit was the nominal $1''$ per pixel. At each of the 20 positions a 9 s exposure was taken. The resulting cadence for the scan, which included the detector readout, was about 3 min 30 s. We fit each profile in the rasters taken between 14:03 and 14:53 with Gaussians. As is shown in Figure 10, the highest densities during this time were observed during an exposure taken at 14:19:14 UT and indicate a pressure in the loop of $\log P = 16.9$. The pressure is an important constraint because it is directly related to the rate at which energy is deposited in the loop. The absolute intensity, in contrast, depends on both the heating rate and the filling factor (e.g., Warren et al. 2008).

2.2. Observations of the Flare Loops

High-temperature flare loops are rooted in the footpoint regions observed with IRIS, RHESSI, and EIS. We can determine the properties of these loops directly through the observations available from XRT, AIA, and EIS. During this time XRT took full-resolution images in the Al-Poly/Open and Be-Thin/Open filter combinations at a cadence of about 120 s. XRT has a plate scale of about $1''$ per spatial pixel. As noted earlier, AIA took full-resolution images in all of the EUV channels at a cadence of about 12 s and EIS executed a sparse raster over the active region. In addition to the Fe XIV

lines discussed previously, EIS recorded the Fe XVI 262.984, Fe XXIII 263.760, and Fe XXIV 192.040 Å.

In Figure 11 we show selected images from XRT and AIA from the small footpoint region near the sunspot penumbra. The temporal evolution of the intensities from this area is shown in Figure 2. As one would expect, the high temperature emission peaks later than the footpoint emission observed with IRIS and RHESSI (Neupert 1968).

The key constraint that we hope to derive from these observations is a quantitative measure of the temperature distribution for the loops connected to the IRIS footpoints. We measure the temperature in two ways, first we compute filter ratios and then we consider the differential emission measure distribution.

For these calculations we consider the XRT, AIA, and EIS intensities in a small region just above the footpoints imaged in the IRIS slit. This is indicated by the black box shown in Figure 11. Ideally we would consider a point at the loop apex, but further away from the footpoints it becomes unclear if all of the high-temperature emission we observe connects to this footpoint region (see the AIA 94 Å image in Figure 1). We expect the temperature gradients in the corona to be relatively flat and it is unlikely that there will be significant differences between the region we have chosen and the actual loop apex. We estimate the length of these loops to be about 40 Mm.

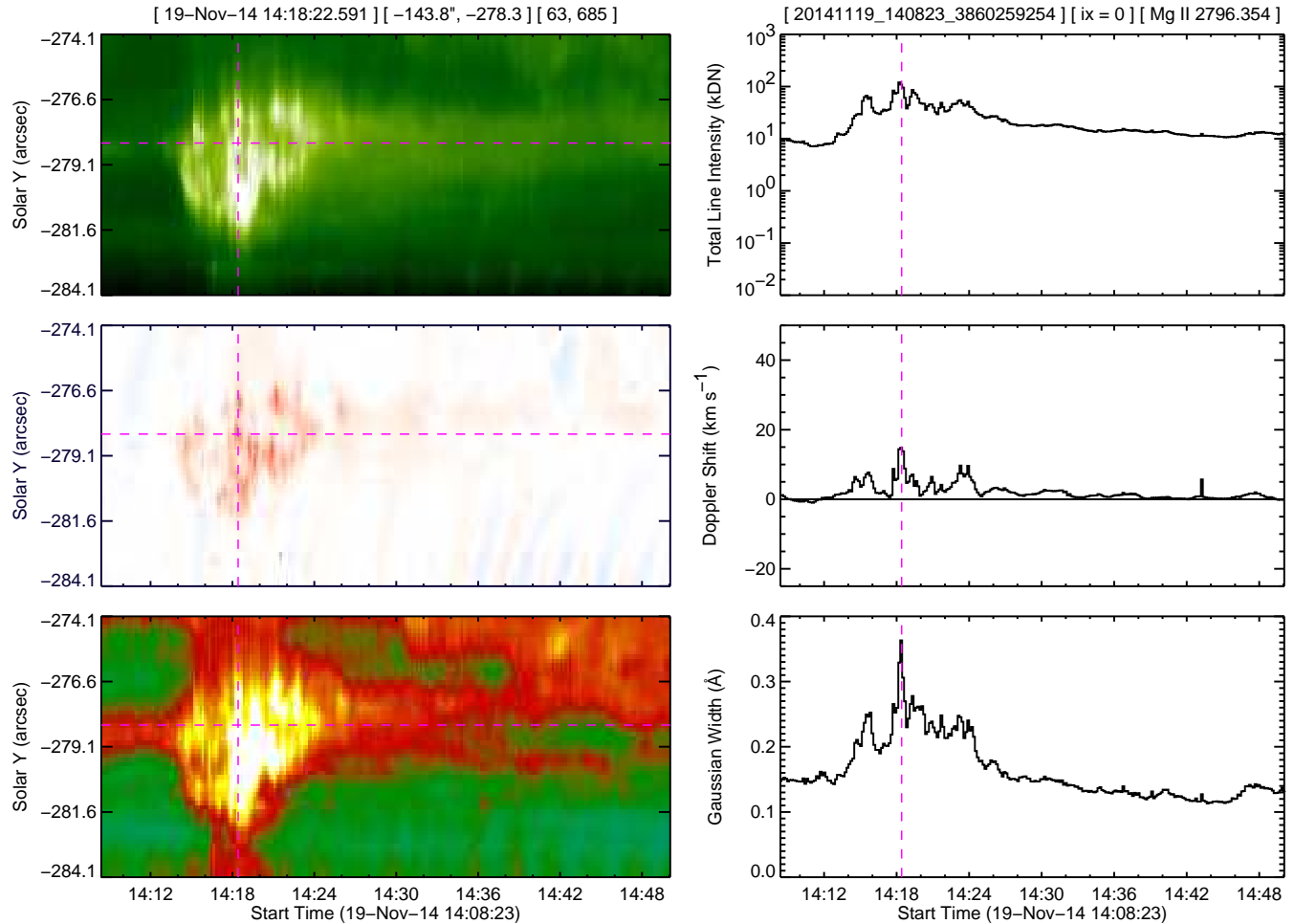


FIG. 8.— The same format as Figure 6 but for the Mg II 2796.354 Å line. The variations in intensity, Doppler shift, and line width are well correlated with those measured for Si IV, but the magnitude of the response is somewhat smaller.

For the filter ratios we consider XRT BeThin/AIPoly and AIA 131/94. As shown in Figure 12, the temperatures derived from these two ratios are generally consistent. The temperatures begin at about $\log T = 7.0$ and decline throughout the event. The AIA filter ratios can be multi-valued and we have chosen the temperature closest to that inferred from XRT. The emission measures derived from these ratios have very similar trends but differ in magnitude by about a factor of 2. We have divided the XRT intensities by 2 to bring the emission measures into agreement with those from AIA.

The fits to the RHESSI spectra shown in Figure 3 indicate somewhat higher temperatures than we have derived from the XRT and AIA filter ratios. These temperatures are not directly comparable since the RHESSI spectra in this analysis are not spatially resolved and the filter ratios are taken from a very small area along a flare loop. We have analyzed the XRT data for the entire field of view of the flare. We obtain a temperature of $\log T \lesssim 7.0$, again smaller than the 13 MK observed with RHESSI, and a volume emission measure of $\log \text{EM} \lesssim 49.3$, which is about three orders of magnitude larger than what is observed with RHESSI. These differences in the temperatures and the magnitudes of the emission measures suggest a distribution of temperatures in the flare loops rather than an isothermal plasma. Further, it suggests that the temperature is likely peaking at about 10 MK and falling

rapidly at higher temperatures.

To estimate the differential emission measure (DEM) in the flare loop of interest we need to invert the equation

$$I_\lambda = \frac{1}{4\pi} \int \epsilon_\lambda(T) \xi(T) dT, \quad (4)$$

where $\epsilon_\lambda(T)$ is the temperature response of the line or band-pass that we have observed to have intensity I_λ and $\xi(T) = n_e^2 ds/dT$ is essentially the distribution of temperatures in the loop. Note that we calculate the differential emission measure distribution but, to facilitate comparisons with the emission measures computed from isothermal models, we plot $\xi(T) dT$.

Inverting this equation requires that we utilize observations over a wide range of temperatures. Ideally we would include EIS intensities in these calculations. While XRT is sensitive to very high temperature emission, Fe XXIII 263.760, and Fe XXIV 192.040 Å provide more localized constraints on the DEM inversion. Significant intensity, however, was observed in these lines in only a few rasters. At most times we observe only background noise. The brightest emission was observed in an exposure taken at 14:22:48 UT and in Figure 13 we show the DEM computed using the intensities of the several EIS emission lines observed at that time. This DEM, which was calculated using the Monte Carlo Markov chain (MCMC) al-

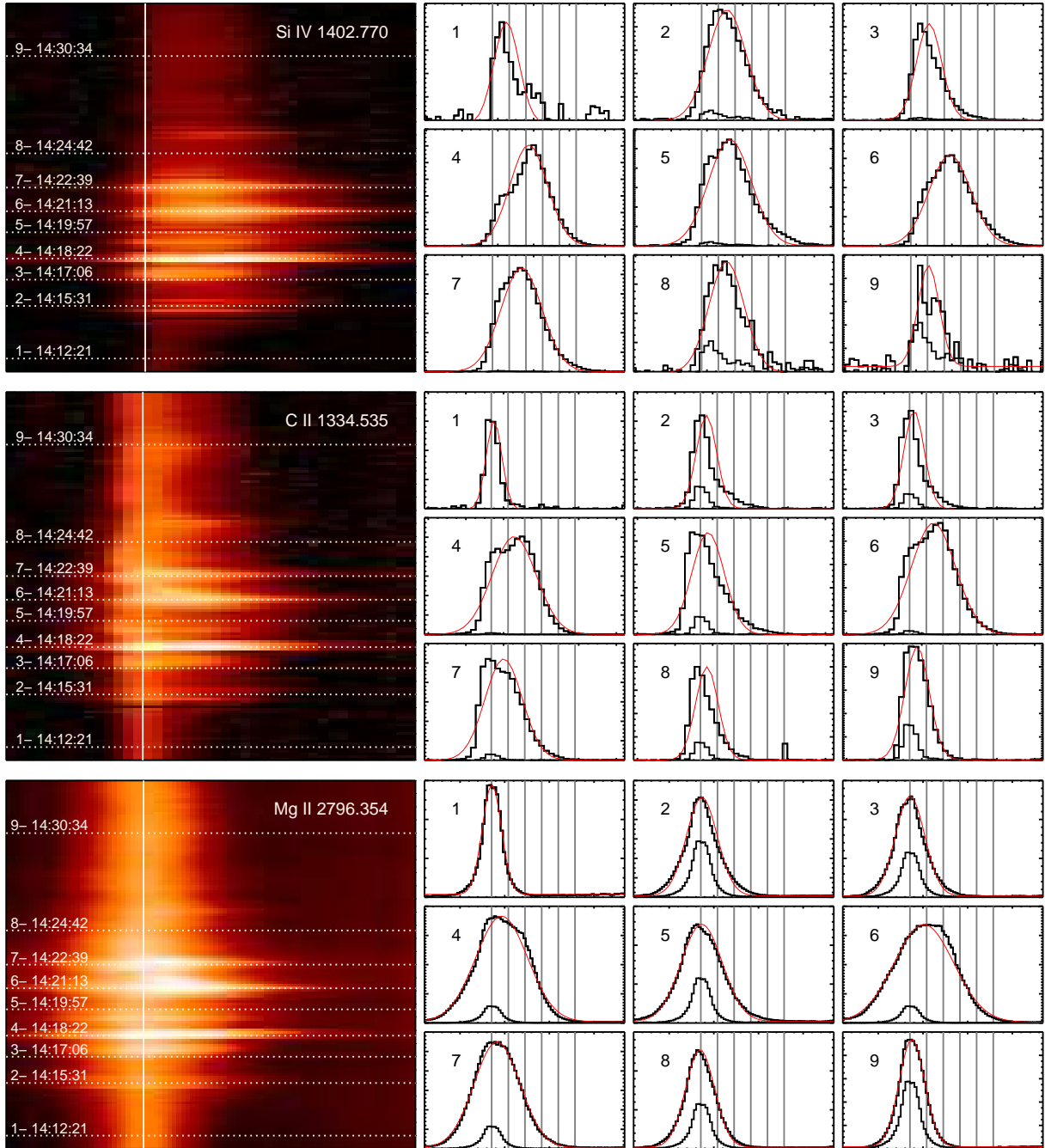


FIG. 9.— IRIS spectra as a function of time for Si IV 1402.770 Å, C II 1334.535 Å, and Mg II 2796.354 Å for a single position. This figure illustrates the multi-component nature of the profiles observed during the flare. The left panels show a stackplot of the spectra while the panels on the right show profiles for selected times. The vertical lines on the spectral profiles are at velocities of 0, 20, 40, 60, 80, and 100 km s⁻¹. Also shown in each profile is the Gaussian profile inferred from the moment calculation. To give a sense of the intensity at each time, a pre-flare profile (#1) is also shown in panels 2–9. The y position for these spectra is indicated by the horizontal line in Figures 6, 7, and 8.

gorithm of Kashyap & Drake (1998), is broadly consistent with the isothermal models discussed previously. It peaks at about 10 MK at falls off at both lower and higher temperatures.

To compute the DEM at all other times when only AIA and XRT are available we include “pseudo intensities” of 0 ± 50 erg cm⁻² s⁻¹ sr⁻¹ for the EIS Fe XXIII 263.760, and Fe XXIV 192.040 Å lines. This biases the DEM to lower values above 10 MK and provides some consistency with the weak signal observed in these lines at most times. Figure 13

shows the DEM computed in this way at three times. The DEM calculated at 14:22:48 UT is broadly consistent with the EIS-only calculation at this time.

Two properties of the DEM are of particular interest: the temperature of the peak and the slope from the peak to lower temperatures. The peak in the DEM will constrain the energy flux. Large energy fluxes will produce high temperatures and it is clear from the observations that the amount of plasma at 10–20 MK is relatively small for this event, as might be expected if the energy fluxes occur on a power-law distribution.

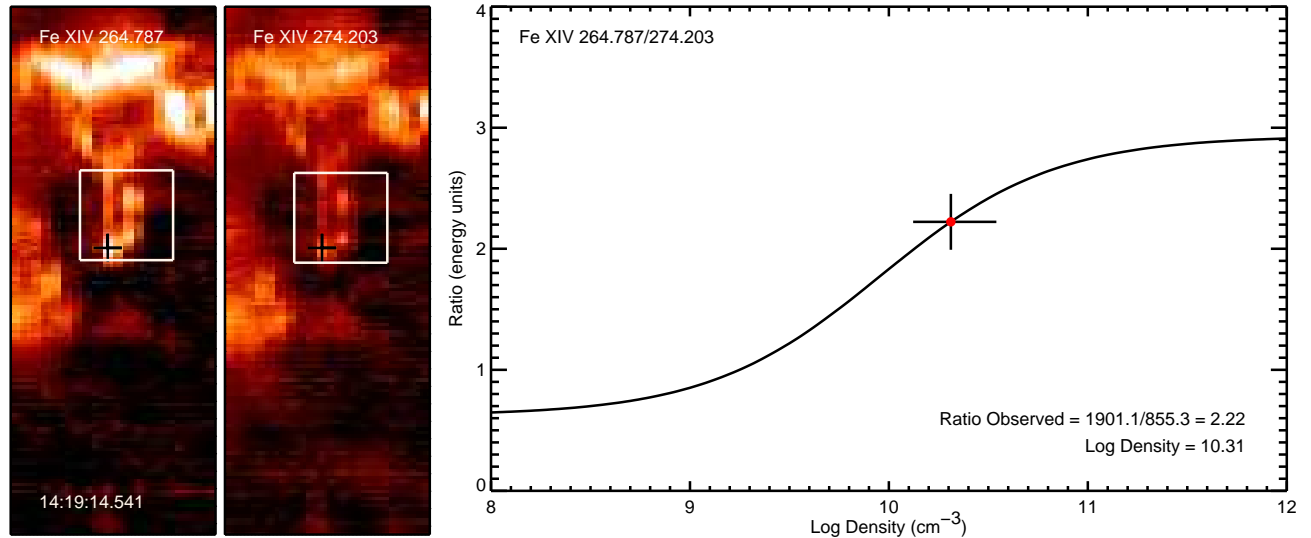


FIG. 10.— The electron density in the footpoint region derived from the EIS Fe XIV density diagnostic. The intensities were measured in an 9 s exposure that began at 14:19:14 UT and indicate a pressure of about $\log P = 16.9$. The intensities have units of $\text{erg cm}^{-2} \text{s}^{-1} \text{sr}^{-1}$.

The slope of the DEM away from the peak is also an important constraint on multi-threaded modeling of the flare. Modeling the event as many small-scale strands that are evolving independently will tend to broaden the DEM and these observations limit that. To make such comparisons more quantitative we have calculated a power-law slope for the EM using a function of the form T^α from the peak to $\log T = 6.2$. Since the MCMC code provides a statistical ensemble of solutions, we fit each one individually and record the median and standard deviation in the results. During the initial part of the flare the slopes are very steep with α typically in the range of 5–6. During the later part of the event cooler plasma is observed, the temperature broadens out, and α is typically in the range of 1–3. Because of the uncertainty in the DEM calculation at temperatures above the peak, we do not consider the high-temperature slope.

3. SUMMARY AND DISCUSSION

We have presented the analysis of a microflare observed with IRIS, RHESSI, AIA, XRT, and EIS. In combination, these observations give us a comprehensive view of both the energy deposition at the flare footpoints, including the properties of the non-thermal electrons and the response of the transition region to the heating that they produce, and the high-temperature loops that form there. At the high spatial and temporal resolution of IRIS we observe that footpoint dynamics are characterized by numerous, small-scale impulsive bursts typically lasting 60 s or less. The resulting distribution of footpoint intensities in the Si IV slit-jaw images follows a power-law with an index of about -1.7. IRIS observations in Si IV, C II, Mg II, and O I allow us to follow the propagation of the energy deposited in the footpoints to lower heights in the solar atmosphere. We observe a progressively weaker response to heating with depth.

The observations from XRT, AIA, and EIS show the formation of high-temperature loops rooted in these footpoints. These loops have a relatively narrow range of temperatures peaked at about 10 MK, consistent with DEMs computed for large flares (e.g., Warren et al. 2013). The comparison of XRT and RHESSI temperatures and emission measures from the full field of view of the event suggests that the temperature

distribution falls very rapidly from 10 MK to 13 MK.

This analysis highlights the difficulty of combining observations with vastly different spatial resolution. For example, the images derived from RHESSI clearly show hard X-ray emission in the vicinity of the footpoint brightenings observed with IRIS. It is not clear, however, if this hard X-ray emission is limited to specific footpoints or covers most of the flare ribbon. The strong correlation between the integrated hard X-ray emission and IRIS footpoint intensities shown in Figure 2 suggests pervasive hard X-ray emission along the flare ribbon, but more observations are needed to confirm this point.

The comprehensive observations provided by IRIS, RHESSI, EIS, XRT, and AIA create an extensive set of requirements for numerical simulations to reproduce. A successful model of this event must account for

1. an increase in Si IV intensity of about 10^3 over the background level that persist for 600 s or more, with smaller increases for C II, Mg II, and O I,
2. red-shifts in Si IV that persist for 600 s or more, with weaker red-shifts in C II and Mg II, and no Doppler shifts for O I,
3. multi-component line profiles for Si IV, C II, and Mg II with little emission at the rest wavelength for Si IV but a significant stationary component for C II and Mg II,
4. DEMs that are sharply peaked near 10 MK or less,
5. loop pressures of about $\log P = 16.9$ (in units of $\text{cm}^{-3} \text{K}$).

We stress that the spectroscopic constraints must be met for an area corresponding to a single IRIS pixel, not the entire flare.

We are currently working on a companion paper (Reep et al. 2016) that focuses on the one-dimensional hydrodynamic modeling of this event with the HYDRODYNAMICS and RADIATION code (HYDRAD; Bradshaw & Mason 2003; Bradshaw & Cargill 2013). Perhaps the most significant challenge presented by these data is the persistent redshifts observed in Si IV and C II. Persistent redshifts have been observed with

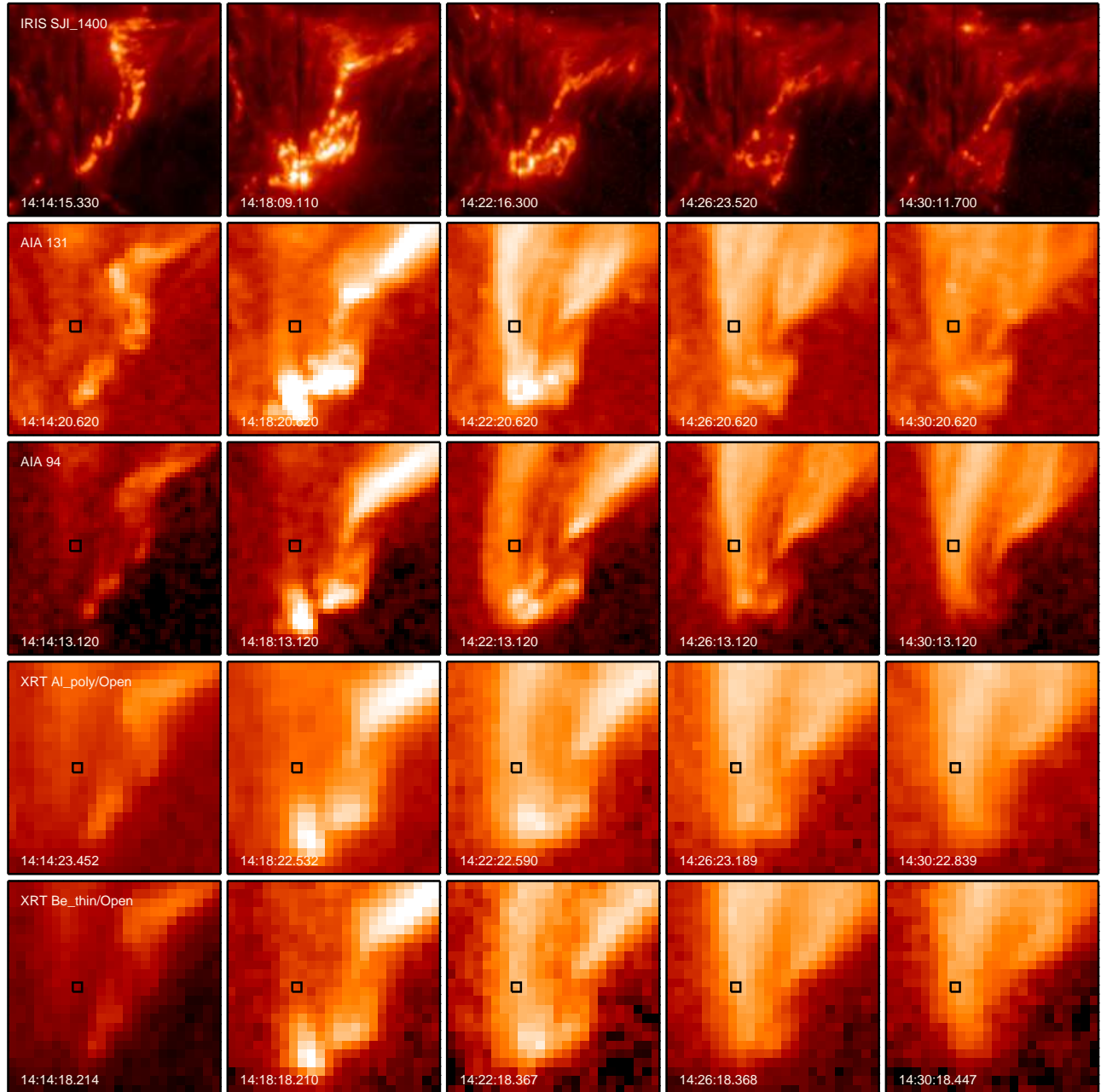


FIG. 11.— Observations of the region around the southern flare footprint with IRIS, AIA, and XRT. The field of view is $26'' \times 26''$ in size.

IRIS for a number of events and are not an idiosyncrasy of the data that we have analyzed (see Brosius & Daw 2015; Brannon et al. 2015; Sadykov et al. 2015; Polito et al. 2016).

It has been known for some time that “chromospheric condensations” accompany evaporative upflows during impulsive flare heating (e.g., Ichimoto & Kurokawa 1984; Zarro et al. 1988; Canfield et al. 1990). These downflows, however, are predicted to dissipate on time-scales of 20–60 s (Fisher 1989), making it difficult to simulate the flows that we observe in a single IRIS pixel with a single loop model. Numerous, small-scale threads appear to be necessary.

This work was supported by NASA’s Hinode project. The research leading to these results has also received funding from the European Community’s Seventh Framework Programme (FP7/2007-2013) under grant agreement no. 606862 (F-CHROMA) (P.J.A.S.). IRIS is a NASA Small Explorer developed and operated by LMSAL with mission operations executed at NASA Ames Research center and major contributions to downlink communications funded by the Norwegian Space Center through an ESA PRODEX contract. CHIANTI is a collaborative project involving George Mason University, the University of Michigan (USA) and the University of Cambridge (UK).

REFERENCES

- Antiochos, S. K., Karpen, J. T., DeLuca, E. E., Golub, L., & Hamilton, P. 2003, *ApJ*, 590, 547
- Antonucci, E., Gabriel, A. H., Acton, L. W., et al. 1982, *Sol. Phys.*, 78, 107

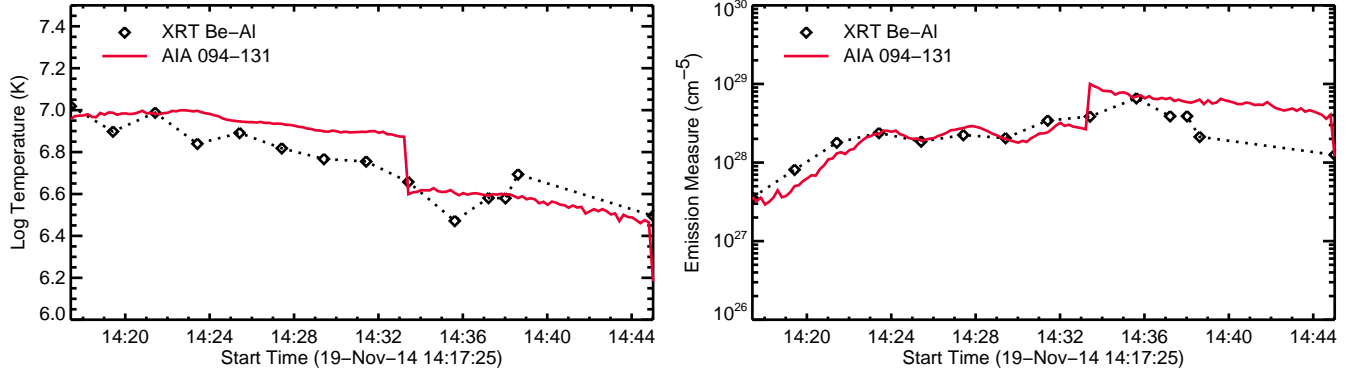


FIG. 12.— XRT and AIA temperatures and emission measures as a function of time derived from XRT BeThin/AIPoly and AIA 131/94 filter ratios. The AIA ratio can be multi-valued and we chose the temperature closest to that derived from the closest XRT measurement. This is the origin of the discontinuity near 14:33.

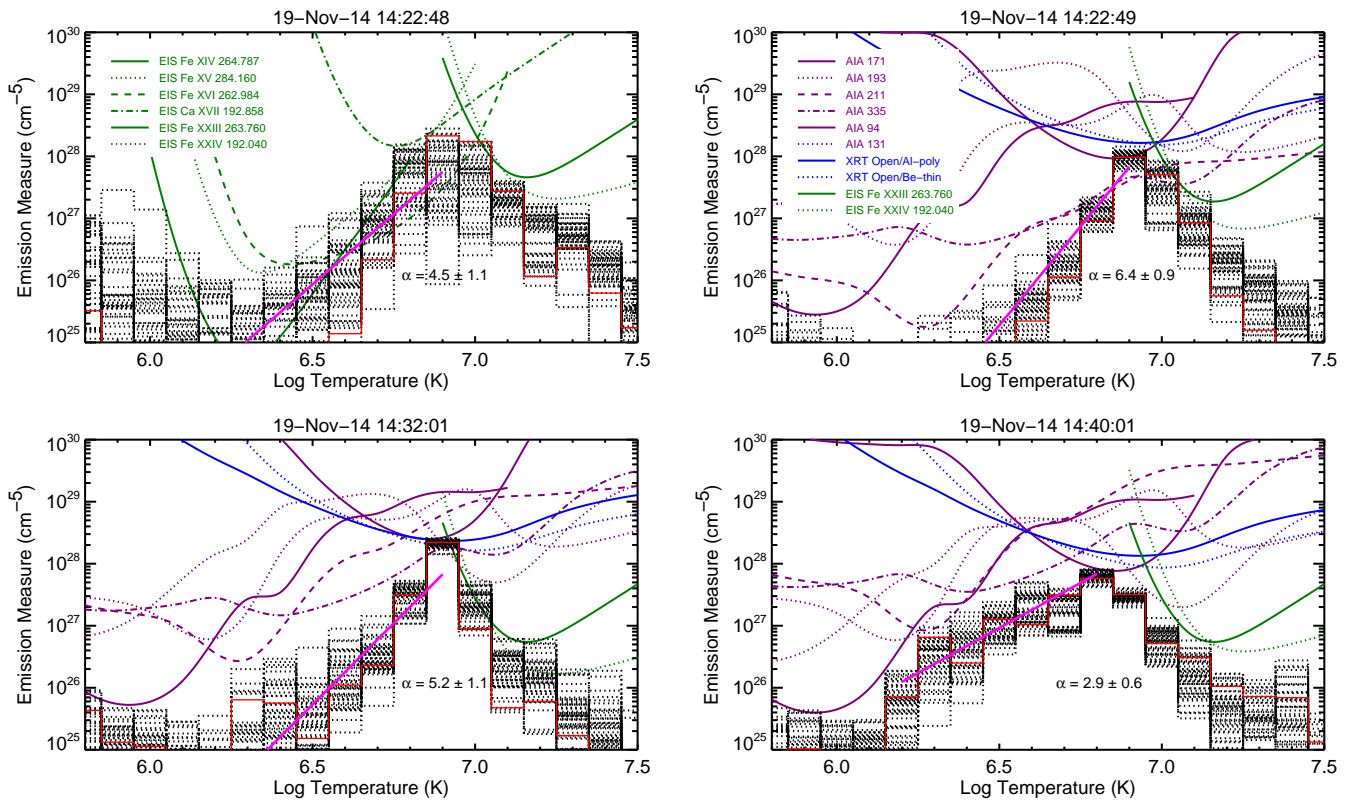


FIG. 13.— The differential emission measure distribution computed from EIS, AIA, and XRT for several times during the event. The distributions generally peak at about 10 MK and fall off sharply at both higher and lower temperatures.

Berger, T. E., de Pontieu, B., Fletcher, L., et al. 1999, *Sol. Phys.*, 190, 409
 Bradshaw, S. J., & Cargill, P. J. 2013, *ApJ*, 770, 12
 Bradshaw, S. J., & Mason, H. E. 2003, *A&A*, 401, 699
 Brannon, S. R., Longcope, D. W., & Qiu, J. 2015, *ApJ*, 810, 4
 Brooks, D. H., & Warren, H. P. 2009, *ApJ*, 703, L10
 Brosius, J. W., & Daw, A. N. 2015, *ApJ*, 810, 45
 Canfield, R. C., Metcalf, T. R., Zarro, D. M., & Lemen, J. R. 1990, *ApJ*, 348, 333
 Cheng, C.-C., Tandberg-Hanssen, E., Bruner, E. C., et al. 1981, *ApJ*, 248, L39
 Cirtain, J. W., Golub, L., Winebarger, A. R., et al. 2013, *Nature*, 493, 501
 Culhane, J. L., Harra, L. K., James, A. M., et al. 2007, *Sol. Phys.*, 243, 19
 Czakowska, A., Alexander, D., & De Pontieu, B. 2001, *ApJ*, 552, 849
 De Pontieu, B., Title, A. M., Lemen, J. R., et al. 2014, *Sol. Phys.*, 289, 2733
 Del Zanna, G., Dere, K. P., Young, P. R., Landi, E., & Mason, H. E. 2015, *A&A*, 582, A56
 Doschek, G. A., Feldman, U., Kreplin, R. W., & Cohen, L. 1980, *ApJ*, 239, 725

Doschek, G. A., Warren, H. P., & Young, P. R. 2013, *ApJ*, 767, 55
 Emslie, G. A., & Alexander, D. 1987, *Sol. Phys.*, 110, 295
 Fisher, G. H. 1989, *ApJ*, 346, 1019
 Fisher, G. H., Canfield, R. C., & McClymont, A. N. 1985, *ApJ*, 289, 425
 Fletcher, L., Dennis, B. R., Hudson, H. S., et al. 2011, *Space Sci. Rev.*, 159, 19
 Golub, L., Deluca, E., Austin, G., et al. 2007, *Sol. Phys.*, 243, 63
 Graham, D. R., & Cauzzi, G. 2015, *ApJ*, 807, L22
 Hori, K., Yokoyama, T., Kosugi, T., & Shibata, K. 1997, *ApJ*, 489, 426
 Hudson, H. S., Strong, K. T., Dennis, B. R., et al. 1994, *ApJ*, 422, L25
 Hurford, G. J., Schmahl, E. J., Schwartz, R. A., et al. 2002, *Sol. Phys.*, 210, 61
 Ichimoto, K., & Kurokawa, H. 1984, *Sol. Phys.*, 93, 105
 Kane, S. R., & Donnelly, R. F. 1971, *ApJ*, 164, 151
 Kashyap, V., & Drake, J. J. 1998, *ApJ*, 503, 450
 Lemen, J. R., Title, A. M., Akin, D. J., et al. 2012, *Sol. Phys.*, 275, 17
 Lin, R. P., Dennis, B. R., Hurford, G. J., et al. 2002, *Sol. Phys.*, 210, 3
 Mariska, J. T., Doschek, G. A., & Bentley, R. D. 1993, *ApJ*, 419, 418

- Mariska, J. T., Emslie, A. G., & Li, P. 1989, *ApJ*, 341, 1067
- Murphy, M. T., & Berengut, J. C. 2014, *MNRAS*, 438, 388
- Nagai, F. 1980, *Sol. Phys.*, 68, 351
- Neupert, W. M. 1968, *ApJ*, 153, L59
- O'Dwyer, B., Del Zanna, G., & Mason, H. E. 2014, *A&A*, 561, A20
- O'Dwyer, B., Del Zanna, G., Mason, H. E., Weber, M. A., & Tripathi, D. 2010, *A&A*, 521, A21
- Pereira, T. M. D., Leenaarts, J., De Pontieu, B., Carlsson, M., & Uitenbroek, H. 2013, *ApJ*, 778, 143
- Poland, A. I., Frost, K. J., Woodgate, B. E., et al. 1982, *Sol. Phys.*, 78, 201
- Polito, V., Reep, J. W., Reeves, K. K., et al. 2016, *ApJ*, 816, 89
- Reep, J. W., Warren, H. P., Crump, N. A., & Simões, P. J. A. 2016, *ApJ*, in preparation
- Reeves, K. K., & Warren, H. P. 2002, *ApJ*, 578, 590
- Sadykov, V. M., Vargas Dominguez, S., Kosovichev, A. G., et al. 2015, *ApJ*, 805, 167
- Schmit, D., Bryans, P., De Pontieu, B., et al. 2015, *ApJ*, 811, 127
- Schwartz, R. A., Csillaghy, A., Tolbert, A. K., et al. 2002, *Sol. Phys.*, 210, 165
- Simões, P. J. A., Graham, D. R., & Fletcher, L. 2015, *Sol. Phys.*, 290, 3573
- Tandberg-Hanssen, E., Reichmann, E., & Woodgate, B. 1983, *Sol. Phys.*, 86, 159
- Testa, P., De Pontieu, B., Martínez-Sykora, J., et al. 2013, *ApJ*, 770, L1
- Testa, P., De Pontieu, B., Allred, J., et al. 2014, *Science*, 346, 1255724
- Tian, H., Li, G., Reeves, K. K., et al. 2014, *ApJ*, 797, L14
- Tian, H., Young, P. R., Reeves, K. K., et al. 2015, *ApJ*, 811, 139
- Warren, H. P. 2006, *ApJ*, 637, 522
- Warren, H. P., Mariska, J. T., & Doschek, G. A. 2013, *ApJ*, 770, 116
- Warren, H. P., Ugarte-Urra, I., Doschek, G. A., Brooks, D. H., & Williams, D. R. 2008, *ApJ*, 686, L131
- Warren, H. P., Winebarger, A. R., & Brooks, D. H. 2012, *ApJ*, 759, 141
- Woodgate, B. E., Shine, R. A., Poland, A. I., & Orwig, L. E. 1983, *ApJ*, 265, 530
- Young, P. R., Tian, H., & Jaeggli, S. 2015, *ApJ*, 799, 218
- Zarro, D. M., Canfield, R. C., Metcalf, T. R., & Strong, K. T. 1988, *ApJ*, 324, 582